

## Differential Cross Sections for Ionization of Laser-Aligned Atoms by Electron Impact

Kate L. Nixon and Andrew James Murray

*Photon Science Institute, School of Physics and Astronomy, University of Manchester, Manchester, United Kingdom*

(Received 5 January 2011; published 21 March 2011)

The first experimental data are given for ( $e, 2e$ ) ionization from laser-aligned atoms. A linearly polarized laser excited Mg atoms to the  $3^1P_1$  state prior to ionization by low energy electrons. The scattered and ejected electrons were detected in coincidence and the differential cross section determined for a range of alignment angles. An asymmetric coplanar geometry was used, with one electron fixed and the other detected at different angles. The data are compared to that from the spherically symmetric  $3^1S_0$  state. Significant differences are found, in both magnitude and angular distribution.

DOI: [10.1103/PhysRevLett.106.123201](https://doi.org/10.1103/PhysRevLett.106.123201)

PACS numbers: 34.80.Dp

The ( $e, 2e$ ) coincidence technique has proven to be highly successful in detailing the collision physics leading to ionization of atomic and molecular targets [1,2]. Experiments define the momentum  $\mathbf{k}_0$  of the incident electron and measure the momenta ( $\mathbf{k}_1, \mathbf{k}_2$ ) of the scattered and ejected electrons using time correlation techniques. Thus, a triple differential cross section (TDCS) is determined. The TDCS ( $\mathbf{k}_0, \mathbf{k}_1, \mathbf{k}_2$ ) is given by solid angles ( $d\Omega_1, d\Omega_2$ ) defining azimuthal ( $\phi_1, \phi_2$ ) and polar ( $\theta_1, \theta_2$ ) angles of the outgoing electrons and by energy conservation relating the incident electron energy ( $E_0$ ) and outgoing electron energies ( $E_1, E_2$ ) to the ionization potential (IP) of the target:

$$\text{TDCS}(\Omega_1, \Omega_2, E_0, E_1, E_2) = \frac{d^3\sigma(E_0)}{d\Omega_1 d\Omega_2 dE_2}, \quad (1)$$

where  $E_0 = \text{IP} + E_1 + E_2$ . The TDCS assumes the target is spherically symmetric, as for all targets prepared in the ground state using conventional techniques, such as from an effusive nozzle or an oven.

For targets that are *prealigned* before ionization, the collision symmetry is reduced, so the cross section must also include the target alignment angle  $d\Omega_T$  ( $\theta_T, \phi_T$ ). In this case a quadruple cross section is required, so that

$$\text{QDCS}(\Omega_T, \Omega_1, \Omega_2, E_0, E_1, E_2) = \frac{d^4\sigma(E_0)}{d\Omega_T d\Omega_1 d\Omega_2 dE_2}, \quad (2)$$

where the IP is now from the aligned state. Measurements of the QDCS are more difficult, since it is necessary to either prealign the target prior to ionization (as presented here) or determine the alignment post collision. Experiments have recently been carried out from aligned  $\text{H}_2$  molecules by observing fragmentation of the  $\text{H}_2^+$  ion following the collision, as occurs when the ion is created in a repulsive state [3–5]. These require a *triple* coincidence measurement between the ion fragment and outgoing electrons to determine the alignment angle and rely on

fragmentation occurring in a time much less than the rotation time of the molecule. The experiments hence have low yield and tend to deliver cross sections with relatively large uncertainties. All have been carried out at high incident energies.

By contrast, no previous ( $e, 2e$ ) experiments have been carried out from laser-aligned *atomic* targets. Weigold and co-workers [6] studied ( $e, 2e$ ) from *oriented* sodium atoms to determine the effect of dichroism, clearly establishing that the target angular momentum plays an important role in the collision dynamics. Photoionization experiments using synchrotron radiation and free electron lasers have also been carried out from laser-aligned targets to study the influence of the target on autoionizing states [7] and double photoionization [8]. In each case lithium was chosen as the target under study.

The most sophisticated quantum models at low energies include convergent close coupling methods [9], time dependent close coupling theories [10], and distorted wave Born approximations and their derivatives [1]. All must include the effects of exchange, target polarization, distortions of the waves describing the electrons and target, and postcollisional interactions. It is in the low energy regime where the largest discrepancies are found between theory and experiment, and so experiments in this regime provide the most exacting test of current models. Recent refinements of theories have improved their accuracy for lighter ground state targets such as He and  $\text{H}_2$ . They also produce reasonable agreement for heavier targets, although some significant discrepancies remain.

These sophisticated models have yet to be rigorously tested for aligned targets, and this is the motivation of the current studies. Further, since atomic alignment leaves the central nucleus unaffected while controlling the momentum  $\mathbf{k}_B$  of the bound electron participating in the collision, this type of reaction is inherently simpler than studying alignment of diatomic and polyatomic molecules, which require the nuclei to be fixed in space. It is hence expected that these new experiments will elucidate important information about collisions with aligned systems, without the

added complexities associated with the spatially distributed nuclei acting as scattering centers.

The  $(e, 2e)$  experiments described here were hence carried out from Mg, which is the lightest alkali-earth target that can be safely studied (and is therefore most amenable to theory). Alkali-earth atoms have the advantage that they have no hyperfine structure, and so can be fully aligned using continuous wave laser radiation coupling the  $n^1S_0$  ground state to the  $n^1P_1$  excited state ( $n = 3$  for Mg) [11]. The experiments were carried out in an asymmetric coplanar geometry, the incident electron momentum  $\mathbf{k}_0$  defining the  $z$  axis. Electron 1 was measured at a fixed angle  $(\theta_1, \phi_1) = (30^\circ, 0)$ ; electron 2 was detected for a range of polar angles  $\theta_2$  on the opposite side of the plane ( $\phi_2 = 180^\circ$ ). The electrons were detected with equal energy  $E_1 = E_2 = 20$  eV using hemispherical energy analyzers located on concentric turntables. The incident electron beam (current  $\sim 5 \mu\text{A}$ ) was produced by an electron gun with a resolution  $\sim 0.6$  eV.

The atomic beam was produced from an oven loaded with high purity Mg. The oven was heated to 840 K on the 1 mm diameter nozzle and 800 K on the body using twin-core heaters. The Mg beam was further collimated by a 1.5 mm diameter aperture located 25 mm above the nozzle. The interaction region defined by the atomic, electron, and laser beams was 18 mm above this output aperture. The Mg beam was collected by a gravity fed liquid nitrogen cold trap 200 mm above the interaction region [12]. The chamber background pressure was  $\sim 2 \times 10^{-7}$  torr with the cold trap filled, and showed no discernible increase when the oven was operating.

Energy selected outgoing electrons were detected in time coincidence using a time to amplitude converter (TAC) operating with a 100 ns window. A National Instruments PCI-6221 card accumulated signal from the TAC to yield coincidence data. This card also operated the stepper motor to move analyzer 2 to a new angle  $\theta_2$ , so that the TDCS and QDCS could be acquired. All systems were monitored, including counts from the analyzers, vacuum pressure, electron beam current, and fluorescence from laser excitation of the Mg atoms.

Laser radiation was provided by a Spectra Physics Matisse DX dye laser and Wavetrain resonant cavity doubler. The fundamental dye laser wavelength was monitored using a High Finesse WSU wave meter. The 285.296458 nm UV beam passed through a beta barium borate (BBO) Glan-laser linear polarizer (extinction  $> 10^4$ ), followed by a zero-order  $\lambda/2$  plate fabricated for this wavelength. The polarization vector of the laser beam was hence varied by rotating the  $\lambda/2$  plate without changing the direction or power of the laser beam. The laser power was 75 mW, with a beam diameter  $\sim 3$  mm at the interaction region.

Alignment of the laser beam was carried out by following a tracer beam from a 650 nm diode laser located behind the electron gun. The tracer beam passed through the gun,

interaction region, Faraday cup, and vacuum chamber window, so the UV beam could be directed collinear with the incident electron beam, but in the opposite direction.

Fluorescence from the interaction region was collected by a 50 mm diameter lens inside the chamber, and was monitored by a SiC quadrant photodiode outside the chamber. Output from the photodiode provided feedback to control the laser wavelength to better than 1 part in  $10^8$ , so as to remain on resonance for several days. This stability was critical to ensure the laser-excited target beam density did not change significantly during data accumulation.

Fine adjustment of the UV-beam position and wavelength was carried out by monitoring *superelastic* electron scattering, as in Fig. 1. This signal arises from electron *deexcitation* of laser-excited atoms, and so only appears when the laser, atomic, and incident electron beams overlap [13]. The analyzer input lenses must also accurately image the interaction region onto the input of the hemispherical energy selectors to produce a signal. The superelastic rate hence provides a precise means to ensure all beams pass through the interaction region. The inelastic spectrum also shows a signature of laser excitation, since a new peak appears at 1.75 eV resulting from *inelastic* scattering from the  $3^1P_1$  laser-excited state to the  $4^1P_1$  state.

By monitoring the superelastic signal, the wavelength to produce maximum laser-excited target density was obtained. In practice, adjustment was an iterative process, so as to maximize yield. Once the superelastic signal was obtained, the laser wavelength was set to be on resonance, and the external photodiode position adjusted to maximize fluorescence. The locking signal from the photodiode was then monitored with the superelastic signal to ensure both peaked together. The photodiode signal was then used to accurately maintain the laser on resonance.

Calibration experiments were performed from the  $3^1S_0$  ground state of Mg (IP = 7.65 eV) to ascertain the TDCS

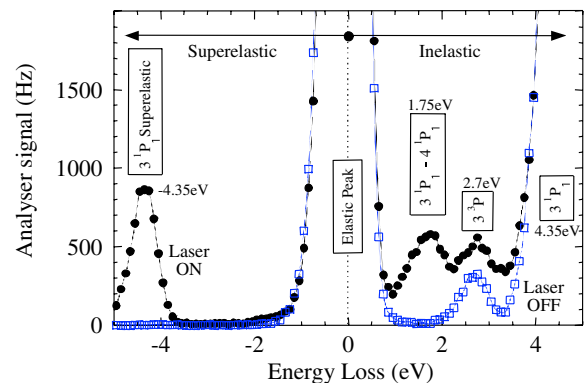


FIG. 1 (color online). Superelastic and inelastic scattering from Mg (closed circles), compared to when the laser is detuned (open squares). The elastic peak defines zero energy. The superelastic peak is clearly resolved at  $-4.35$  eV. A new peak appears at  $\sim 1.75$  eV due to electron scattering from laser-excited targets.

under the same conditions as for the excited state. The analyzers were set to detect 20 eV electrons and a binding energy spectrum taken to establish contact potentials within the apparatus. These are principally due to the filament work function, but may also arise from deposition of Mg onto surfaces. A contact potential of  $\sim 1.4$  eV was found, which was unchanged for both ground and excited state experiments. The energy resolution of the coincidence signal was  $\sim 1$  eV, due to the combined resolution of the gun and analyzers. For ground state ionization the electron gun was hence set to 46.25 eV to allow for this contact potential, whereas for ionization from the laser-excited state the incident electron beam energy was reduced by 4.34 eV (the excitation energy of the  $4^1P_1$  state). The coincidence resolution of the spectrometer ( $\sim 1$  eV) could hence easily resolve the excited state signal from that arising from the ground state.

Figure 2 shows the resulting TDCS normalized to unity at the peak, which occurs at  $\theta_2 = 55^\circ$ . The TDCS shows a dominant forward peak, the structure having a FWHM of  $\sim 27^\circ$ . A minimum occurs at  $\theta_2 \sim 105^\circ$ , which is  $\sim 1.5\%$  of the peak. This type of forward scattering is often observed, and at high energy arises due to a binary collision so that the TDCS peaks along the momentum transfer direction  $\mathbf{q} = \mathbf{k}_0 - \mathbf{k}_1$ . In the present experiments  $\mathbf{q}$  is at  $\theta_2 = 36.4^\circ$ , indicating that additional factors such as post-collisional interactions strongly influence the interaction.

An important consideration for laser experiments is the relative population of excited targets  $\rho_T^{\text{laser}}(t)$  produced prior to the collision. This can be determined by both modeling the laser interaction [14] and by measuring the relative change in the TDCS from the ground state when the laser is off and on resonance. The QDCS magnitude can then be measured relative to the TDCS, for comparison to theory.

For these experiments a quantization axis was chosen along the laser beam, in the direction  $-\mathbf{k}_0$ . The linearly polarized laser beam is then described as a coherent superposition of left- and right-hand circular radiation, so only

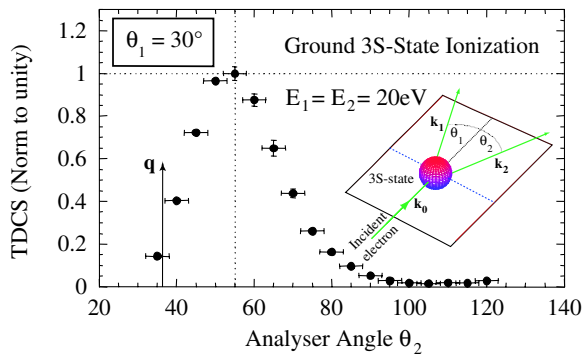


FIG. 2 (color online). TDCS from the spherically symmetric 3S-ground state of Mg for outgoing energies  $E_1 = E_2 = 20$  eV, with  $\theta_1 = 30^\circ$ . The TDCS is normalized to unity at the peak, which occurs at  $\theta_2 \sim 55^\circ$ . The direction of the momentum transfer  $\mathbf{q} = \mathbf{k}_0 - \mathbf{k}_1$  is shown.

the  $m_J = \pm 1$  substates of the  $3^1P_1$  state are excited. The laser-excited state can be described by a density matrix [11]:

$$\rho_{3^1P_1}^{\text{laser}}(t) = \frac{\rho_T^{\text{laser}}(t)}{2} \begin{pmatrix} 1 & 0 & e^{+2i\varepsilon} \\ 0 & 0 & 0 \\ e^{-2i\varepsilon} & 0 & 1 \end{pmatrix}, \quad (3)$$

where  $\rho_T^{\text{laser}}(t)$  defines the relative population of excited targets compared to the ground state, and  $\varepsilon$  is the angle of the laser polarization with respect to the scattering plane. For the experiments described here, the alignment angles are given by  $(\theta_T, \phi_T) = (90^\circ, \varepsilon)$ . In the absence of magnetic fields,  $\varepsilon$  does not depend on time. By contrast,  $\rho_T^{\text{laser}}(t)$  displays Rabi oscillations over a period of  $\sim 30$  ns before reaching steady state. This period is short compared to the time atoms are in the laser beam ( $\sim 3 \mu\text{s}$ ), and so to a good approximation  $\rho_T^{\text{laser}}(t)$  can be replaced by the steady state population  $\rho_T^{\text{SS}}$  so that

$$\rho_T^{\text{laser}} \approx \rho_T^{\text{SS}} = \frac{4\eta^2 I_{\text{laser}}}{8\eta^2 I_{\text{laser}} + \Gamma_e^2 + 4\delta^2}, \quad (4)$$

where  $I_{\text{laser}}$  is the laser beam intensity ( $\text{mW}/\text{mm}^2$ ),  $\Gamma_e^{-1} = 2.04$  ns the  $3^1P_1$  state lifetime,  $\delta$  detuning from resonance of the radiation (due to the Doppler profile), and  $\eta = 8.28 \times 10^7$ , a constant defining the coupling of the laser radiation to the atoms [11].

Equations (3) and (4) define the initial target state and population of laser-excited atoms in the interaction region. Under the conditions described here, a population of 25%–27% of the ground state was calculated. This was verified by experiments which measured the change in the TDCS from the ground state when the laser was on and off resonance. The reduction with the laser on resonance was found to be  $26\% \pm 4\%$ , confirming the calculation. This population was then used to relate the QDCS magnitude to the TDCS.

Figure 3 shows the measured QDCS for  $\varepsilon = 0^\circ, 45^\circ$ , and  $90^\circ$  normalized to the TDCS in Fig. 2 so as to reflect an equivalent density of laser-excited and ground state atoms in the interaction region. Normalization to the ground state TDCS was accomplished by multiplying the data from the excited states by  $0.26^{-1}$ . Cross-normalization between results for laser excitation was carried out by repeating the experiment for each  $\varepsilon$  at  $\theta_2 = 50^\circ$ , so that a relative scale and uncertainty could be determined. The relative uncertainty in the normalization between data sets compared to the ground state was hence calculated to be  $\pm 9\%$  ( $\varepsilon = 0^\circ$ ),  $\pm 7\%$  ( $\varepsilon = 45^\circ$ ), and  $\pm 22\%$  ( $\varepsilon = 90^\circ$ ).

Several features are striking about the results in Fig. 3. Most significantly, the QDCS with  $\varepsilon = 0^\circ$  is observed to be 13% larger than the TDCS at the peak. The FWHM is slightly narrower at  $\sim 22^\circ$ , peaking at  $\theta_2 \sim 57.5^\circ$ . There appears to be a minimum at  $\theta_2 \sim 115^\circ$  with a magnitude  $\sim 1.4\%$  of the peak, but this is not as clear as for the ground state. For  $\varepsilon = 45^\circ$  the QDCS peaks at 97% of the TDCS and again maximizes at  $\theta_2 \sim 55^\circ$ , but the FWHM has

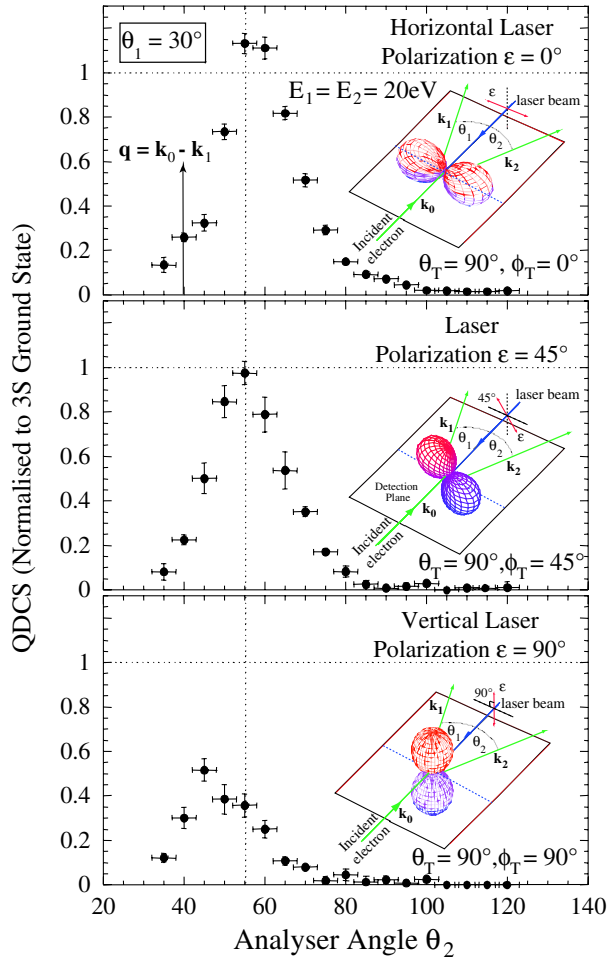


FIG. 3 (color online). QDCS for alignment angles  $\varepsilon = 0^\circ$ ,  $45^\circ$ , and  $90^\circ$  of the  $3P$  state, normalized to the TDCS in Fig. 2. The uncertainty in the relative normalization compared to the ground state is  $\pm 9\%$  for  $\varepsilon = 0^\circ$ ,  $\pm 7\%$  for  $\varepsilon = 45^\circ$ , and  $\pm 22\%$  for  $\varepsilon = 90^\circ$ .

reduced to  $\sim 20^\circ$ . A shallow minimum is observed at  $\theta_2 \sim 90^\circ$  with a magnitude  $\sim 1\%$  of the peak. The cross section at higher angles is very small, so no obvious second peak is observed.

For  $\varepsilon = 90^\circ$  the peak has shifted to  $\theta_2 \sim 45^\circ$  and has reduced to 51% of the TDCS. The forward peak appears to show a slight “double peak” structure with a shallow dip at  $\sim 50^\circ$ , as often seen for  $p$  electrons due to their momentum distribution [2]. A minimum appears at  $\theta_2 \sim 75^\circ$  with a magnitude  $\sim 4\%$  of the peak, but the statistics for data at these higher angles are again relatively poor due to low count rates. The FWHM is  $\sim 20^\circ$ , as for measurements with  $\varepsilon = 45^\circ$ .

One of the key differences between the  $3S$  ground state and the laser-excited  $3P$  state is that the  $3S$  state is spherically symmetric (the bound electron has no given direction in space) and the electron momentum peaks at zero. By

contrast, the momentum  $\mathbf{k}_B$  of the aligned  $3P$  electron peaks at nonzero values and has a well-defined direction given by  $\varepsilon$ . When  $\varepsilon \neq 0^\circ$   $\mathbf{k}_B$  lies out of the scattering plane, so the component  $\mathbf{k}_B^\perp$  perpendicular to the plane must be carried from the reaction by the ion. In particular, when  $\varepsilon = 90^\circ$  there is no component  $\mathbf{k}_B^\parallel$  in the scattering plane. Multiple scattering must then occur for the electrons to be detected in this plane, in an analogous way to that seen in perpendicular plane studies [15]. However, if the process was elastic scattering from the nucleus followed by a binary collision in the scattering plane (as describes perpendicular plane results), the QDCS peak would be expected to occur at  $\theta_2 \approx 90^\circ - \theta_1 = 60^\circ$ , rather than at  $45^\circ$  as observed. Clearly more complex interactions are occurring in the reactions detailed here.

For a full description it is essential to develop new theories which consider an aligned target state and then calculate the QDCS from fundamental principles. The existing low energy theories are well placed to explore this new area of research, and it will be interesting to see how accurately they predict the TDCS and QDCS presented here.

Future experiments will carry out a systematic study with  $\varepsilon$  varying in the scattering plane (by directing the laser beam orthogonal to the plane) and through further out of plane studies. It will also be interesting to observe the reaction when the outgoing electrons carry *unequal* energy. It is hoped experiment can be guided by theory in the near future, as the QDCS depends on many parameters, and so a theoretically directed approach will allow the sensitivity of the reaction to different initial conditions to be fully explored.

We acknowledge the Photon Science Institute central laser facility for supplying the laser system used here.

- [1] D.H. Madison and O. Al-Hagan, *J. At. Mol. Opt. Phys.* **2010**, 367180 (2010).
- [2] I.E. McCarthy and E. Weigold, *Rep. Prog. Phys.* **54**, 789 (1991).
- [3] M. Takahashi *et al.*, *Phys. Rev. Lett.* **94**, 213202 (2005).
- [4] S. Bellm *et al.*, *Phys. Rev. Lett.* **104**, 023202 (2010).
- [5] A. Senftleben *et al.*, *J. Chem. Phys.* **133**, 044302 (2010).
- [6] A. Dorn *et al.*, *Phys. Rev. Lett.* **80**, 257 (1998).
- [7] M. Meyer *et al.*, *Phys. Rev. Lett.* **59**, 2963 (1987).
- [8] G. Zhu *et al.*, *Phys. Rev. Lett.* **103**, 103008 (2009).
- [9] D.V. Fursa *et al.*, *Phys. Rev. A* **80**, 022717 (2009).
- [10] J. Colgan *et al.*, *J. Phys. B* **42**, 145002 (2009).
- [11] A.J. Murray *et al.*, *Phys. Rev. A* **77**, 013409 (2008).
- [12] A.J. Murray, *Meas. Sci. Technol.* **13**, N12 (2002).
- [13] M.J. Hussey *et al.*, *Phys. Rev. Lett.* **99**, 133202 (2007).
- [14] A.J. Murray *et al.*, *Meas. Sci. Technol.* **17**, 3094 (2006).
- [15] O. Al-Hagan *et al.*, *Nature Phys.* **5**, 59 (2008).